

This manuscript version is made available under the CC-BY-NC-ND 4.0 license <http://creativecommons.org/licenses/by-nc-nd/4.0/>

## **Title**

# **9.4% efficient Cu<sub>2</sub>ZnSnSe<sub>4</sub> solar cells from co-sputtered elemental metal precursor and rapid thermal annealing**

C. Andres \*, S. G. Haass, Y. E. Romanyuk, A. N. Tiwari

Laboratory for Thin Films and Photovoltaics, Empa – Swiss Federal Laboratories for Materials Science and Technology, Ueberlandstrasse 129, 8600 Duebendorf, Switzerland

\* Corresponding author: e-mail: christian.andres@empa.ch, Phone: +41 58 765 48 17, Fax: +41 58 765 40 42

## **Abstract**

We present a fast fabrication route for Cu<sub>2</sub>ZnSnSe<sub>4</sub> (CZTSe) kesterite absorbers using co-sputtering of elemental metal precursor followed by rapid thermal annealing with selenium capping layers. The formation of secondary phases at the absorber surface can be reduced, making a specific etching routine redundant. Starting from a homogenous metal precursor with Se capping layer, a short annealing time of 5 min at 550°C is sufficient to achieve fully crystallized kesterite absorber. Selenium capping layers with thickness at least twice the precursor thickness were found to yield very homogenous absorber on 5x5 cm<sup>2</sup> samples but also promote the formation of ZnSe. By reducing the Se layer thickness an enhanced grain growth and reduction of secondary phases can be achieved, which finally yields maximum efficiencies up to 9.4%.

**Keywords:** thin films solar cells, kesterite, sputtering, rapid thermal processing.

## 1. Introduction

Due to the abundance of its constituents, kesterite solar cells ( $\text{Cu}_2\text{ZnSn}(\text{S,Se})_4$ ) (CZTSSe) are considered to be a sustainable alternative to highly efficient chalcopyrite ( $\text{Cu}(\text{In,Ga})(\text{S,Se})_2$ ) (CIGS) solar cells. Currently, the efficiency of kesterite solar cells is still limited to 12.6% for CZTSSe [1] and 11.6% for the sulphur-free CZTSe [2], mainly attributed to a large deficit in open circuit voltage. Sputtering of metal precursor with subsequent annealing is a robust synthesis route for thin film absorber offering high throughput and excellent process control. For pure selenide absorber, efficiencies over 10% could be achieved for stacked metal precursors [3],[4]. The spatial separation of the constituents in the stacked precursor can promote phase segregation, thus, longer annealing times are needed to ensure complete intermixing or different etchants have to be used to remove residual secondary phases [5],[6],[7]. To overcome the issue of intermixing of metals in the precursor, direct co-sputtering [8] and stacking of multiple thin layers were recently employed [9],[10], reaching efficiencies up to 8.1% [11]. In this study, we follow the approach of co-sputtering mixed metal precursor and investigate the influence of an evaporated selenium capping layer on the morphology, grain growth and formation of secondary phases of the annealed absorber. We show that it is possible to significantly reduce secondary phases using rapid thermal annealing by tuning the thickness of the selenium capping layer, which makes an additional etching step redundant. The consequences on the final device performance are discussed and an efficiency of 9.4% for the best cell is demonstrated.

## 2. Experimental details

The Mo back contact was deposited using DC sputtering on top of soda lime glass with  $\text{SiO}_x$  as the alkali diffusion barrier. A mixed Cu-Zn-Sn precursor was deposited by co-sputtering of elemental metal targets (Cu: 99.999%, 3.6 W/cm<sup>2</sup>; Zn: 99.995%, 2.9 W/cm<sup>2</sup>; Sn: 99.999%, 4.0 W/cm<sup>2</sup>) at room temperature in a con-focal arrangement (AJA ATC-Orion 5 system from AJA Inc.). The precursor composition with  $\text{Cu}/(\text{Zn}+\text{Sn}) = 0.75$  and  $\text{Zn}/\text{Sn} = 1.35$  was deduced from the individual sputter rates and confirmed by energy-dispersive X-ray (EDX) measurements. A sputtering time of 12.5 min under an Ar base pressure of 0.26 Pa resulted in a precursor thickness of 400 nm. For all experiments, the same

metal precursor recipe was used. Prior to the annealing, a Se capping layer of various thicknesses was thermally evaporated on top of the unheated metal precursor in order to reduce elemental losses [10] and enhance homogeneity during the annealing. In a rapid thermal processing (RTP) system (AS-ONE from Annealsys), the precursor was heated to 550°C for 5 minutes with additional Se pellets (800 mg) in a closed graphite reactor. The annealing was performed using a nitrogen base pressure of 625 mbar and fast heating and cooling rates (from room temperature to 550°C at a rate of 4°C/s and cooling from 550°C to 300°C in 5 min).

As deposited CZTSe absorber were subsequently covered with a CdS buffer by chemical bath deposition without further surface treatment, followed by the deposition of the i-ZnO/ZnO:Al window by RF magnetron sputtering. In the final step a Ni/Al grid was applied by e-beam evaporation and individual cells (0.36 cm<sup>2</sup>) were mechanically scribed. No anti-reflection coating was applied. The morphology was studied by scanning electron microscopy (SEM, HITACHI S-4800) and combined with energy-dispersive X-ray spectroscopy (EDX, 7 kV and 20 kV acceleration voltage, emission current 10 µA) to reveal surface composition. The bulk composition was determined by using X-ray fluorescence (XRF, 45 kV acceleration voltage). X-ray diffraction (XRD) pattern were recorded using Cu K<sub>α</sub> radiation (Bruker D8). Depth profiling data were obtained with a time-of-flight Secondary Ion Mass Spectroscopy (SIMS) 5 system from ION-TOF. Bi<sup>+</sup> ions were used as primary ions and positive ions were detected. Sputtering was performed using O<sub>2</sub><sup>+</sup> sputtering ions with 2 keV ion energy, 400 nA ion current and a 300×300 µm<sup>2</sup> raster size. An area of 100×100 µm<sup>2</sup> was analyzed using Bi<sup>+</sup> ions with 25 keV ion energy. Raman scattering measurements were performed with FHR640 Horiba-Jobin Yvon spectrometer coupled to Raman probe developed at IREC and -70°C cooled CCD detector. Backscattering measurements using a 442 nm monochromatic laser line from the HeCd gas laser as excitation sources. The laser power density was kept below 250W/cm<sup>2</sup> in order to avoid thermal effect. In order to characterize a representative area of the samples' surface, a spot diameter of 50 µm was used. All measurements were calibrated spectrally using a silicon monocrystalline reference, imposing the position of the main band at 520 cm<sup>-1</sup>.

The CZTSe solar cell devices were characterized by current–voltage (JV) and external quantum efficiency (EQE) measurements under standard test conditions (AM 1.5G spectrum, 25 °C, 1000 W/m<sup>2</sup>).

### 3. Results and discussion

#### 3.1. Precursor analysis

The co-sputtered precursor appears as uniform metallic layer with silver color. The SIMS depth profile (Fig. 1) proves that Cu, Zn and Sn are evenly distributed within the whole precursor depth. To analyze the phase composition of the precursor, each of the constituents of the mixed precursor was solely sputtered on molybdenum using identical deposition parameters as for co-sputtering. The XRD patterns of Cu/Mo, Zn/Mo and Sn/Mo stacks were measured and are depicted in Fig. 1. When analyzing the XRD pattern of the mixed CZT precursor, it can be clearly seen that no elemental Cu and Zn exist in the mixed precursor while Sn is present. The formation of different brass and bronze phases takes place during deposition at room temperature. Small traces of ZnO are visible, which form presumably during the storage in air. The residues of Sn were also reported for precursors from thin multilayer arrangement [12].

#### 3.2. Absorber analysis

RTP of the precursor was performed using samples with 1.15, 0.85, 0.57, and 0.28  $\mu\text{m}$  thick Se capping layers and additional Se pellets. Fig. 2a) shows a representative XRD pattern of a completed solar cell device processed from a 1.15  $\mu\text{m}$  Se top layer. It exhibits all typical reflections for the CZTSe phase and reveals the presence of  $\text{MoSe}_2$ . No characteristic peaks of Cu-Se and Sn-Se phases could be observed. The CZTSe peaks present a shoulder towards smaller angles. The origin could be the presence of ZnSe,  $\text{Cu}_2\text{SnSe}_3$  or related to stress. However, a clear discrimination by XRD is not possible [13]. The inset in Fig. 2a) represents the (011) reflection of CZTSe absorbers synthesized from different selenium layer thicknesses. No effect on full width-at-half-maximum (FWHM) and reflection intensity can be observed for the investigated range of Se top layer thicknesses. Figure 2b) and 2c) show the SIMS depth profile for absorber synthesized with 1.15  $\mu\text{m}$  and 0.57  $\mu\text{m}$  Se top layer, respectively. A comparison of the absorbers reveals a significant increase in Zn counts at the surface in the case of a thicker Se top layer, which can be attributed to a segregation of ZnSe at the absorber surface. It is worth noting that the SIMS signals are less abrupt at the absorber/Mo interface than at the precursor/Mo interface because of absorber roughness. In Fig. 3 segregations of ZnSe appear in SEM top view images as bright spots, which is confirmed by EDX mapping and point measurements. Due to the initial very Zn-rich precursor, the composition of the CZTSe phase remains still Zn-rich despite the phase segregation. SEM top view

and cross section images presented in Fig. 4 a)-d) gives further evidence about secondary phases and morphology. The increasing amount of ZnSe on the absorber surface for increasing Se layer thickness is supported by surface sensitive EDX (increasing Zn/Sn ratio), while XRF bulk measurements remain unaffected as shown in Table 1. Depending on the grain size, the thickness of the absorber varies between 1-1.5  $\mu\text{m}$  as estimated from the SEM cross section images. The use of rather thick Se layer was found to be beneficial for the lateral homogeneity on 5x5  $\text{cm}^2$  absorber, which can be seen from the macroscopic appearance as well as the distribution of JV parameters. On the other hand, exceeding a certain excess of the selenium layer, detrimental effects on the microscopic morphology like the formation of ZnSe, reduced grain size and increased surface roughness can be observed. The grain size increases when increasing the Se layer thickness from d) 0.28  $\mu\text{m}$  to c) 0.57  $\mu\text{m}$ , but further decreases for higher amounts of selenium a) and b) due to the segregation of ZnSe. While liquid Se is reported to enhance the grain growth [14], the segregation of ZnSe seems to hinder the grain growth of the CZTSe crystals. Further experiments are needed to understand the segregation of ZnSe in dependency of the capping layer thickness. Raman characterization of the complete devices using the 442nm excitation wavelength (2.8eV) is showed in the Fig 5. The characterization under blue light and the bandgap difference of the ZnO:Al/i-ZnO/CdS windows layers allows to evaluate the presence of the ZnSe phase in the surface of the absorber by the Raman signal enhancement induced for the resonant conditions for the ZnSe ( $E_g \approx 2.6\text{eV}$ ). The ratio of the ZnSe signal contributions with the main peaks of the CZTSe allows observe a variation of the ZnSe concentration in the absorber surface (penetration depth in the absorber estimated  $< 50\text{ nm}$ ). Further evaluations of the CZTSe main modes indicate a Zn-rich composition for samples with thicker Se top layer, which is expressed in a decrease in intensity of the B mode around  $170\text{ cm}^{-1}$  and a broadening of the A mode around  $197\text{ cm}^{-1}$  [15].

### 3.3. Solar cell parameters

To evaluate the influence of morphology, surface roughness and formation of ZnSe on the final device performance, JV measurements for 49 cells scribed on 5x5 $\text{cm}^2$  samples with a cell area of  $0.36\text{ cm}^2$  were performed (Fig. 6). As mentioned earlier, reducing the thickness of the Se top layer deteriorated the lateral homogeneity of the sample, which was manifested in a larger spread of the JV parameters. The inhomogeneity arose mainly from pinholes in the absorber, which led to low shunt resistance of

the devices. Shunting was more pronounced in the center region of the device, while cells located closer to the edges were not affected. When comparing the best cells, it is obvious that fill factor and short-circuit current increase when the formation of ZnSe is suppressed. The open-circuit voltage is less dependent on the morphology and has similar values. Despite the lack of homogeneity, the best cell was obtained using a 0.57  $\mu\text{m}$  Se top layer. The JV curve and the detailed device parameters for the best cell are given in Fig. 7. The cell achieves a  $V_{\text{OC}}$  of 440 mV, a  $J_{\text{SC}}$  of 34.0  $\text{mA}/\text{cm}^2$  and a fill factor of 63.0% resulting in a cell efficiency of 9.4%. The short-circuit current was calculated from integration of the EQE spectrum (Fig. 7). No light-soaking effect was observed for these cells. A bandgap value of 1.06 eV was derived from the inflection point of the EQE curve.

#### **4. Conclusion**

A combination of co-sputtered metal precursor with evaporated Se top layer and a rapid thermal annealing was exploited to synthesize CZTSe absorbers. A selenium top layer can be used to reduce elemental losses and improve homogeneity. The high reactivity of elemental metals with selenium allows a very short annealing time of 5 min to achieve well-crystallized kesterite absorbers. Using this fabrication route, it is possible to achieve efficiencies over 9% without any further surface treatment. We show the strong influence of the selenium supply on the formation of ZnSe, grain growth and device performance. Tuning the Se top layer thickness adequately, the appearance of ZnSe on the absorber surface can be strongly reduced.

#### **Acknowledgements**

Dr. Victor Izquierdo-Roca from IREC, Catalonia Institute for Energy Research is gratefully acknowledged for performing the Raman measurements and detailed discussion of the results. Financial support from the Swiss National Science Foundation (SNF) in the network of the Indo-Swiss Joint Research Programme (ISJRP) is gratefully acknowledged. The authors would like to thank the whole team of the Laboratory for Thin Films and Photovoltaics.

## References

- [1] W. Wang, M.T. Winkler, O. Gunawan, T. Gokmen, T.K. Todorov, Y. Zhu, D.B. Mitzi, Device Characteristics of CZTSSe Thin-Film Solar Cells with 12.6% Efficiency, *Adv. Energy Mater.* 4 (2014) 1301465.
- [2] Y.S. Lee, T. Gershon, O. Gunawan, T.K. Todorov, T. Gokmen, Y. Virgus, S. Guha,  $\text{Cu}_2\text{ZnSnSe}_4$  Thin-Film Solar Cells by Thermal Co-evaporation with 11.6% Efficiency and Improved Minority Carrier Diffusion Length, *Adv. Energy Mater.* 5 (2015) 1401372.
- [3] S. Oueslati, G. Brammertz, M. Buffière, H. ElAnzeery, O. Touayar, C. Köble, J. Bekaert, M. Meuris, J. Poortmans, Physical and electrical characterization of high-performance  $\text{Cu}_2\text{ZnSnSe}_4$  based thin film solar cells, *Thin Solid Films.* 582 (2015) 224.
- [4] S. Giraldo, M. Neuschitzer, T. Thersleff, S. López-Marino, Y. Sánchez, H. Xie, M. Colina, M. Placidi, P. Pistor, V. Izquierdo-Roca, K. Leifer, A. Pérez-Rodríguez, E. Saucedo, Large Efficiency Improvement in  $\text{Cu}_2\text{ZnSnSe}_4$  Solar Cells by Introducing a Superficial Ge Nanolayer, *Adv. Energy Mater.* 5 (2015) 1501070.
- [5] M. Bär, B.-A. Schubert, B. Marsen, S. Krause, S. Pookpanratana, T. Unold, L. Weinhardt, C. Heske, H.-W. Schock, Impact of KCN etching on the chemical and electronic surface structure of  $\text{Cu}_2\text{ZnSnS}_4$  thin-film solar cell absorbers, *Appl. Phys. Lett.* 99 (2011) 152111.
- [6] S. López-Marino, Y. Sánchez, M. Placidi, A. Fairbrother, M. Espindola-Rodríguez, X. Fontané, V. Izquierdo-Roca, J. López-García, L. Calvo-Barrio, A. Pérez-Rodríguez, E. Saucedo, ZnSe Etching of Zn-Rich  $\text{Cu}_2\text{ZnSnSe}_4$ : An Oxidation Route for Improved Solar-Cell Efficiency, *Chem. Eur. J.* 19 (2013) 14814.
- [7] H. Xie, Y. Sánchez, S. López-Marino, M. Espíndola-Rodríguez, M. Neuschitzer, D. Sylla, A. Fairbrother, V. Izquierdo-Roca, A. Pérez-Rodríguez, E. Saucedo, Impact of Sn(S,Se) Secondary Phases in  $\text{Cu}_2\text{ZnSn(S,Se)}_4$  Solar Cells: a Chemical Route for Their Selective Removal and Absorber Surface Passivation, *ACS Appl. Mater. Interfaces.* 6 (2014) 12744.
- [8] R. Bodeux, F. Mollica, S. Delbos, Growth of  $\text{Cu}_2\text{ZnSnSe}_4$  by cosputtering and reactive annealing atmosphere, *Sol. Energy Mater. Sol. Cells.* 132 (2015) 67.
- [9] J. Márquez-Prieto, Y. Ren, R.W. Miles, N. Pearsall, I. Forbes, The influence of precursor Cu content and two-stage processing conditions on the microstructure of  $\text{Cu}_2\text{ZnSnSe}_4$ , *Thin Solid Films.* 582 (2015) 220.
- [10] R. Lechner, S. Jost, J. Palm, M. Gowtham, F. Sorin, B. Louis, H. Yoo, R.A. Wibowo, R. Hock,  $\text{Cu}_2\text{ZnSn(S,Se)}_4$  solar cells processed by rapid thermal processing of stacked elemental layer precursors, *Thin Solid Films.* 535 (2013) 5.

- [11] J. Márquez, M. Neuschitzer, M. Dimitrievska, R. Gunder, S. Haass, M. Werner, Y.E. Romanyuk, S. Schorr, N.M. Pearsall, I. Forbes, Systematic compositional changes and their influence on lattice and optoelectronic properties of  $\text{Cu}_2\text{ZnSnSe}_4$  kesterite solar cells, *Sol. Energy Mater. Sol. Cells.* 144 (2016) 579.
- [12] R.A. Wibowo, H. Yoo, A. Hölzing, R. Lechner, S. Jost, J. Palm, M. Gowtham, B. Louis, R. Hock, A study of kesterite  $\text{Cu}_2\text{ZnSn}(\text{Se},\text{S})_4$  formation from sputtered Cu–Zn–Sn metal precursors by rapid thermal processing sulfo-selenization of the metal thin films, *Thin Solid Films.* 535 (2013) 57.
- [13] P. M. P. Salomé, P. A. Fernandes, J. P. Leitão, M. G. Sousa, J. P. Teixeira, and A. F. da Cunha, Secondary crystalline phases identification in  $\text{Cu}_2\text{ZnSnSe}_4$  thin films: contributions from Raman scattering and photoluminescence, *J. Mater. Sci.* 49 (2014) 7425.
- [14] A. R. Uhl, P. Fuchs, A. Rieger, F. Pianezzi, C. M. Sutter-Fella, L. Kranz, D. Keller, H. Hagendorfer, Y. E. Romanyuk, F. LaMattina, S. Yoon, L. Karvonen, T. Magorian-Friedlmeier, E. Ahlswede, D. VanGenechten, F. Stassin, and A. N. Tiwari, Liquid-selenium-enhanced grain growth of nanoparticle precursor layers for  $\text{CuInSe}_2$  solar cell absorbers, *Prog. Photovolt. Res. Appl.* 23 (2015) 1110.
- [15] M. Dimitrievska, A. Fairbrother, E. Saucedo, A. Pérez-Rodríguez, and V. Izquierdo-Roca, Influence of compositionally induced defects on the vibrational properties of device grade  $\text{Cu}_2\text{ZnSnSe}_4$  absorbers for kesterite based solar cells, *Appl. Phys. Lett.* 106 (2015) 73903.



## Figures

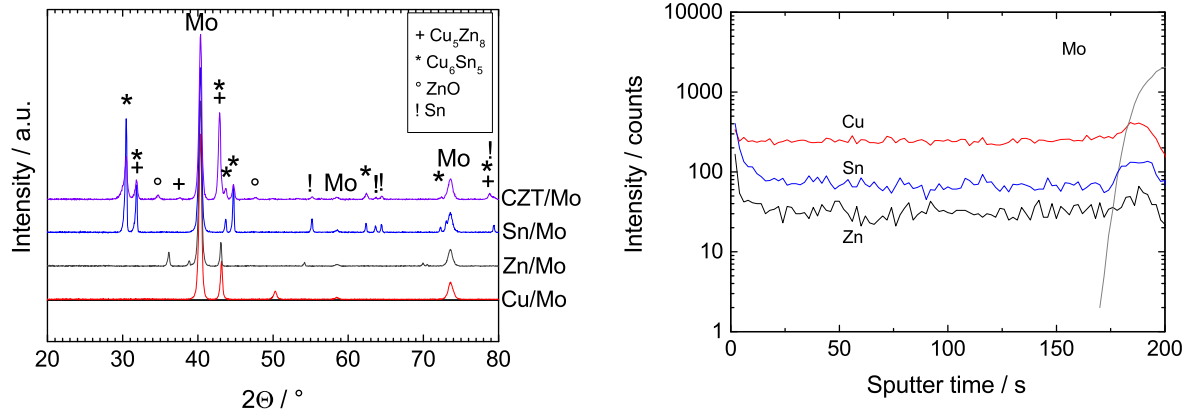


**Fig. 1:** *Left:* XRD profiles for sputtered CZT/Mo, Sn/Mo, Zn/Mo and Cu/Mo stacks. For the CZT/Mo stack reflections for Cu-Zn and Cu-Sn alloys as well as elemental Sn and traces of ZnO are detected. *Right:* SIMS depth profile of the CZT/Mo stack. Cu, Zn and Sn are evenly distributed through the whole precursor thickness.

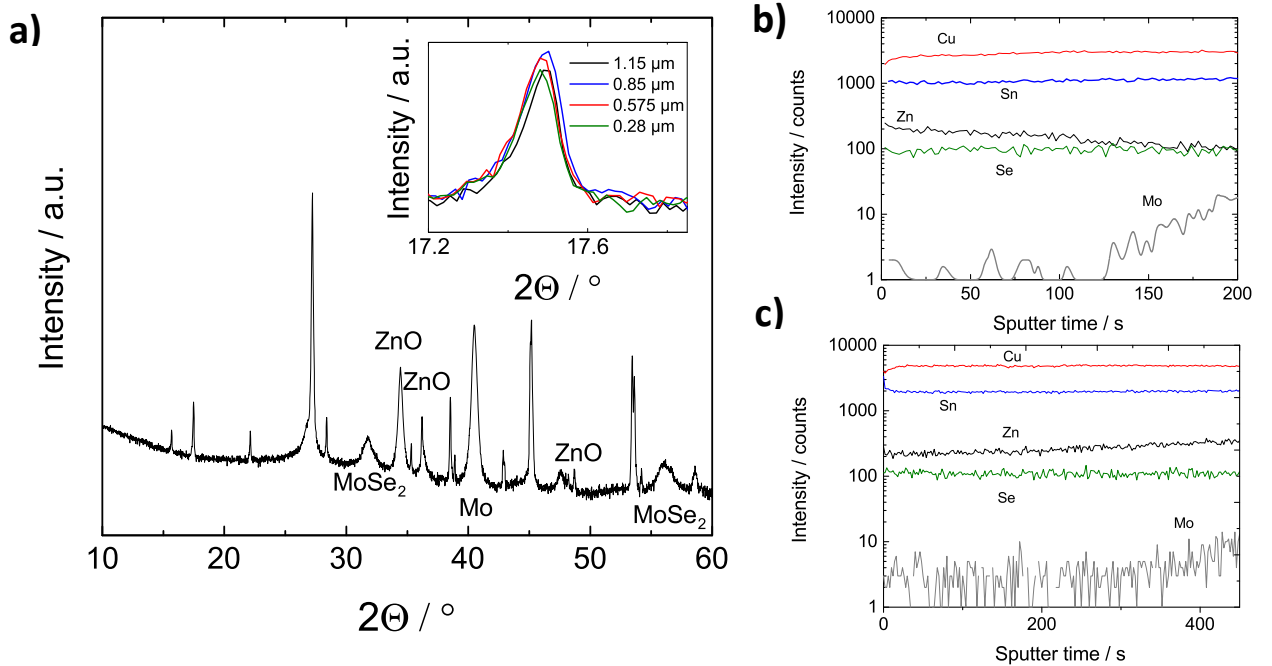


**Fig. 2:** *a):* XRD profile for a complete solar cell from co-sputtered elemental precursor. The data is plotted in logarithmic intensity scale to highlight present reflections. The inset shows a comparison of the (011) reflection for absorbers synthesized from different Se top layer thicknesses. No significant changes in intensity and FWHM can be observed. *b,c):* SIMS depth profile of a CZTSe absorber synthesized with *b)* 1.15  $\mu\text{m}$  and *c)* 0.57  $\mu\text{m}$  Se top layer. The interface

between absorber and back contact is not abrupt due to a high roughness of the CZTSe layer. In case of b), an increase of Zn counts at the front is observed due to the ZnSe phase segregation.

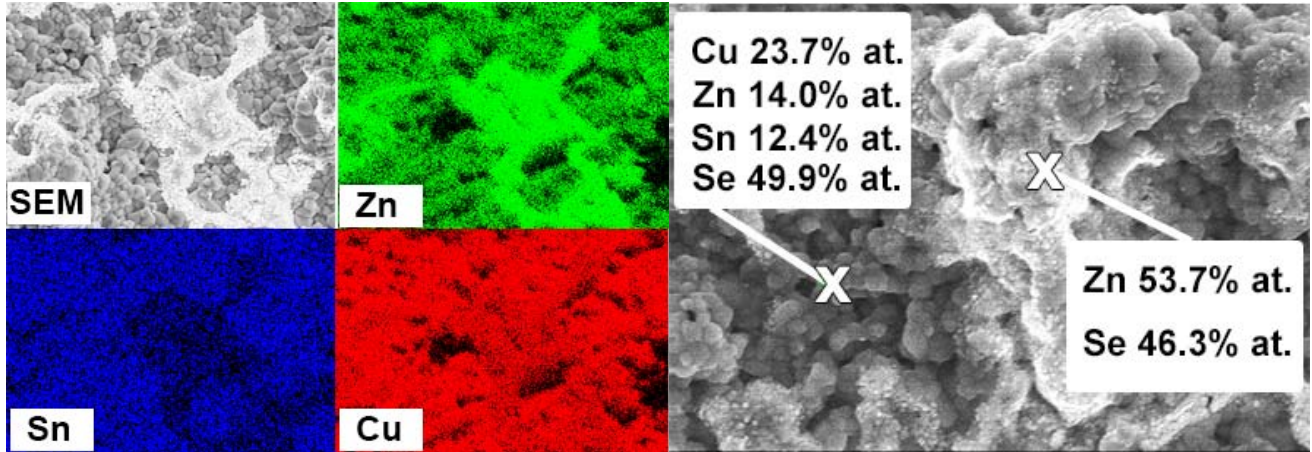


**Fig. 3:** *Left:* EDX mapping of an absorber surface with 1.15  $\mu\text{m}$  Se top layer. The bright appearing spots in the SEM image show a high intensity in Zn signal, which can be correlated with the formation of ZnSe. *Right:* EDX point measurements at “dark” and “bright” spots, revealing the composition of the CZTSe phase and the segregated ZnSe phase.

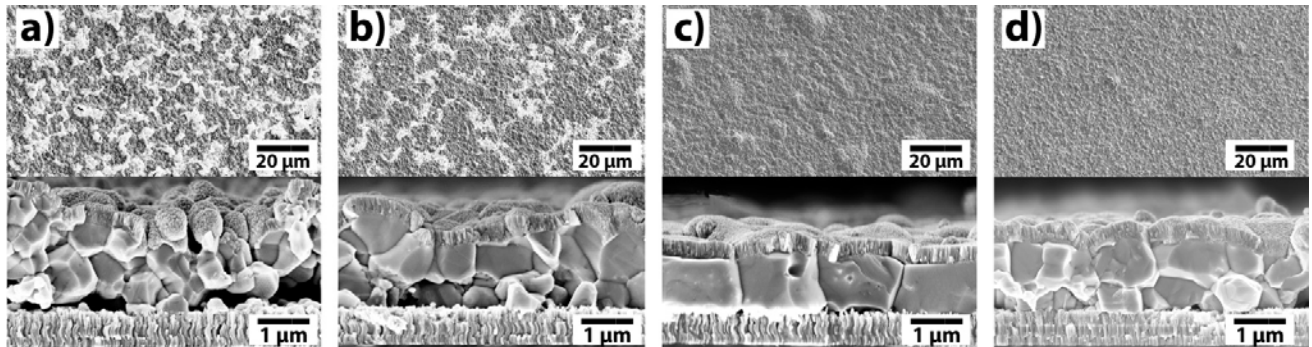


**Fig. 4:** *Top:* SEM top view of bare absorber synthesized with different Se top layer thicknesses: a) 1.15  $\mu\text{m}$  b) 0.85  $\mu\text{m}$  c) 0.575  $\mu\text{m}$  d) 0.28  $\mu\text{m}$  *Bottom:* SEM cross section of the complete solar cell synthesized with different Se top layer thicknesses: a) 1.15  $\mu\text{m}$  b) 0.85  $\mu\text{m}$  c) 0.575  $\mu\text{m}$  d) 0.28  $\mu\text{m}$ .

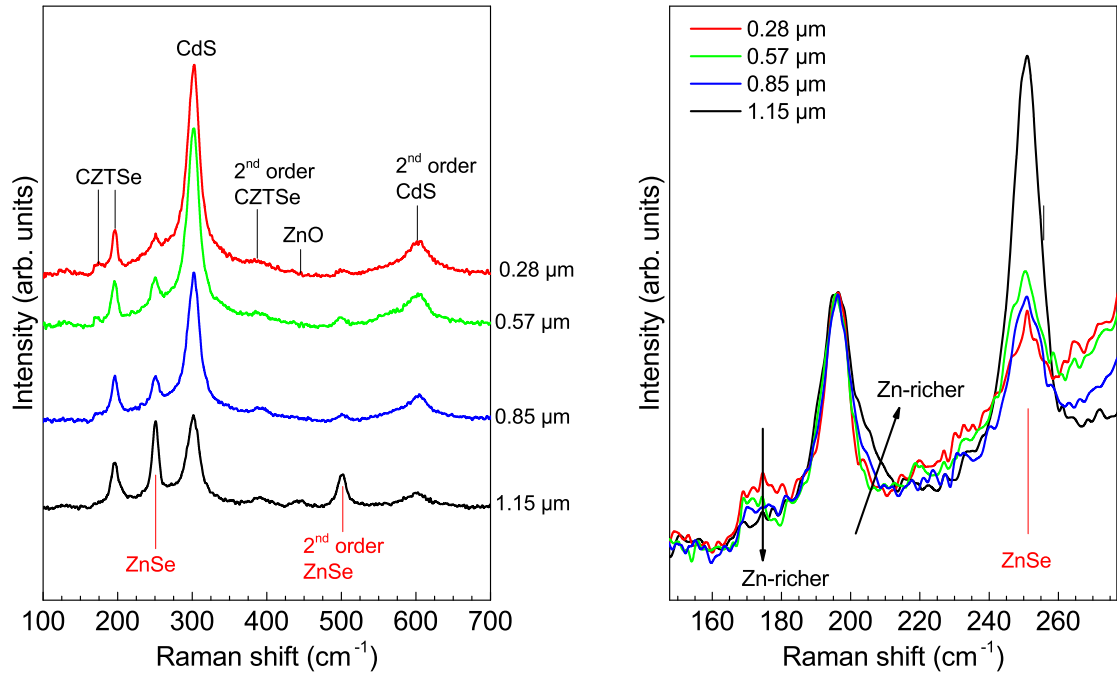


**Fig. 5:** *Left:* Raman spectra of completed devices with different Se top layer thickness. *Right:* Detailed view of 1<sup>st</sup> order CZTSe and ZnSe peaks. Arrows indicate increase of Zn content. All spectra are measured with 442 nm excitation wavelength.

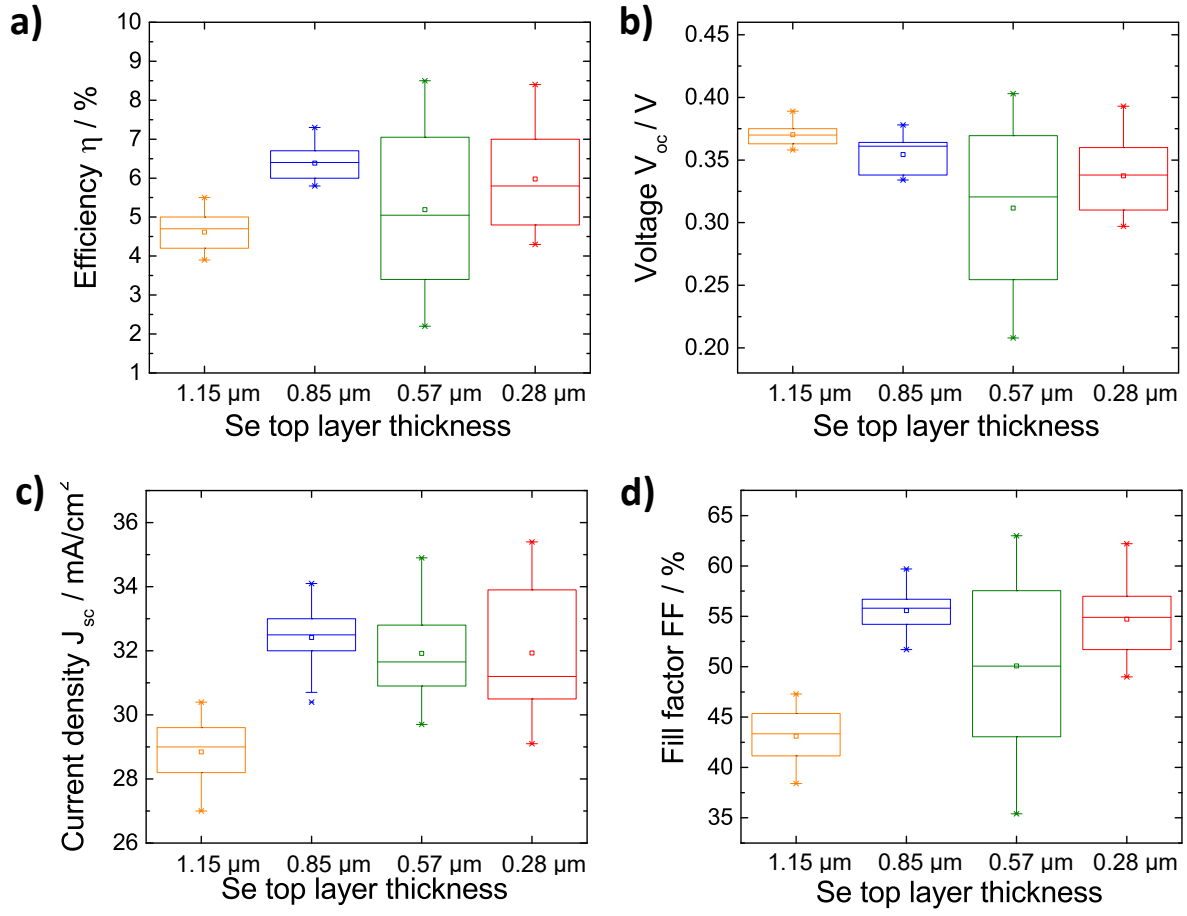


**Fig. 6:** *a)* Efficiency, *b)* open-circuit voltage, *c)* short-circuit current density and *d)* fill factor of solar cells synthesized from different Se top layer thicknesses. The graphs represent best, average and median values obtained from 49 solar cells of 0.36 cm<sup>2</sup> area each located on 5x5 cm<sup>2</sup> substrates.

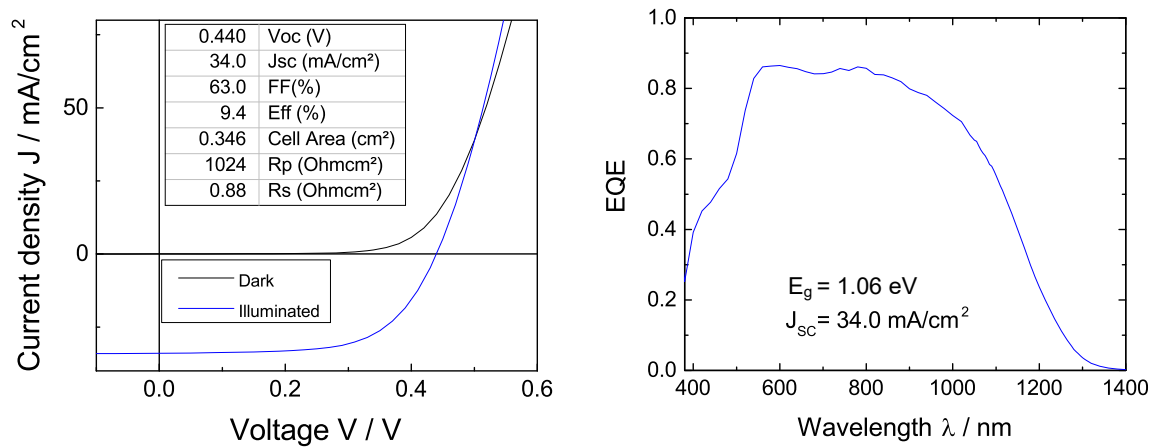


**Fig. 7:** *Left:* Solar cell parameters for the best cell (0.575  $\mu$ m Se layer thickness) without anti-reflection coating. *Right:* External quantum efficiency measurement for the best cell without anti-reflection coating.

**Table 1:** Comparison of compositional measurements (EDX and XRF) for samples with different Se top layer thicknesses. The surface sensitive EDX measurements reveal higher zinc content for samples with thicker Se capping layer, while XRF measurements show no significant differences in bulk composition.

		1.15 $\mu$ m	0.85 $\mu$ m	0.57 $\mu$ m	0.28 $\mu$ m
EDX	Cu/(Zn+Sn)	0.69	0.75	0.74	0.81
	Zn/Sn	1.45	1.30	1.18	1.14
XRF	Cu/(Zn+Sn)	0.81	0.83	0.83	0.80
	Zn/Sn	1.29	1.25	1.28	1.24